Research Article | Vol. 27, No. 22 / 28 October 2019 / Optics Express 31225
Optics EXPRESS

850 nm GaAs/AlGaAs DFB lasers with shallow surface gratings and oxide aperture

PENGFEI ZHANG,[1] CAN LIU,[1] MINWEN XIANG,[1] XIANG MA,[1] GONGYUAN ZHAO,[1] QIAOYIN LU,[1,*] JOHN F. DONEGAN,[2] AND WEIHUA GUO[1]

[1] *Wuhan National Laboratory for Optoelectronics, and School of Optical and Electronic Information, Huazhong University of Science and Technology, 1037 Luoyu Road, Wuhan 430074, China*
[2] *School of Physics, CRANN and CONNECT, Trinity College Dublin, Dublin 2, Ireland*
[*] *luqy@hust.edu.cn*

Abstract: We present and experimentally demonstrate a novel oxide-confined ridge-waveguide distributed feedback (DFB) laser with the first-order surface grating using only a single growth step. The metal contacts are laterally offset from the ridge waveguide to inject current thus avoiding unwanted light absorption from the electrodes. The oxide aperture is defined by selective wet oxidation of aluminium-rich material, which confines the injection current from the electrodes to the active layer under the ridge waveguide. This allows that a thin ridge layer can be used with relatively higher refractive index compared to the active layer and thus the grating can be shallowly etched but provides a strong coupling effect. The fabricated 150 μm-long DFB laser exhibited a relatively low threshold current of 8 mA and a side mode suppression ratio (SMSR) up to 50 dB at the injected current of 32 mA around 4 times threshold at 20 °C. Stable single mode operation has been observed for the fabricated DFB laser over the temperature range from 10 to 50 °C. The variation of wavelength with temperature $\Delta\lambda/\Delta T$ was 0.06 nm/°C. The proposed laser may have advantages combined both DFB lasers and vertical-cavity surface-emitting lasers (VCSELs), such as single mode, stabilized polarization, potentially narrow linewidth and low power consumption. In addition, the laser is regrowth free, thus has advantages of low cost and high reliability.

1. Introduction

Semiconductor distributed feedback lasers in the GaAs-AlGaAs material system are attractive sources for many applications including optical communication system, and pump sources for quantum sensors [1–4]. Of particular importance is the development of single-mode, single polarization, low threshold, low power consumption and narrow linewidth optical sources for atomic clocks [5], laser cooling [6], interferometers [7], light detection and ranging (LIDARs) [8].

Generally there are two kinds of laser schemes to realize the above sources. One is the VCSEL and another is the side (edge) emitting laser. VCSELs have advantages of low threshold and low power consumption due to their very small laser cavities [9–10]. However, VCSELs generally have disadvantages such as low output power and difficulty to realize a high side-mode suppression ratio (SMSR) [10–12]. VCSELs' linewidth is also generally wide at around 100 MHz due to the inherently short photon lifetime in a typical VCSEL cavity [13]. In addition, VCSELs don't have a well-defined polarization direction and generally require additional approaches to stabilize the polarization [14–15].

The edge emitting lasers generally use different approaches to integrate gratings so as to realize single mode working. To avoid the problem of AlGaAs oxidation, the buried grating DFB laser was realized by implementing p-GaAsP and p-InGaP grating layers [16]. Also Al-free buried grating DFB lasers were proposed with an active layer of a GaAsP [17] and GaInAsP [18]

#372932 https://doi.org/10.1364/OE.27.031225
Journal © 2019 Received 22 Jul 2019; revised 29 Aug 2019; accepted 3 Sep 2019; published 14 Oct 2019

Optics EXPRESS

quantum well structure. The edge emitting lasers based on surface gratings have been presented for many years including laterally coupled grating lasers [19–20] and vertically coupled grating lasers [21–24]. Recently, laterally coupled surface grating lasers with narrow linewidth have been demonstrated using nanoimprint lithography [25–27]. However, the lateral coupled grating generally suffered from a weak coupling effect on the optical waveguide mode [25]. The vertical coupled grating normally has a trade-off between the absorption loss caused by the metal contacts on the top of gratings and the coupling overlap with optical waveguide mode in the active layer [23]. To decrease the loss but increase the coupling effect, surface grating lasers with higher order vertically coupled gratings have been recently demonstrated by carefully defining V-shaped grating trenches [28], however, the process is relative complex. These edge emitting lasers have advantages of single mode, single polarization, good SMSR and relatively narrow linewidth. However, the threshold of these lasers is generally high when compared with VCSELs. Other than this, the lateral-current-injection DFB (LCI-DFB) lasers [29] with a surface grating structure was demonstrated, which has a high index-coupling coefficient and low power consumption [30]. However, the LCI-DFB lasers require complex regrowth techniques [29].

In this work, we propose a novel scheme of oxide-aperture confined ridge-waveguide DFB laser with first-order surface gratings using conventional AlGaAs materials for potentially low threshold based on a single epitaxial growth. There is no metallization on the ridge waveguide. The metal contacts are laterally offset from the ridge waveguide to inject current, thus avoiding unwanted light absorption from the electrodes. The oxide aperture is defined by selective wet oxidation of aluminium-rich material, which confines the injection current from the electrode to the active layer under the ridge waveguide. This allows that a thin ridge layer can be used with relatively high refractive index compared to the active layer and thus the grating can be shallowly etched (~ 100 nm deep) but provides a strong coupling effect. It predicts that the presented laser can potentially work with low threshold at a short cavity length. Relatively low threshold current and stable single mode operation have been demonstrated for the fabricated 150 μm-long DFB lasers of the first run.

2. Device structure and fabrication

2.1. Device structure

The proposed DFB laser is a surface ridge waveguide laser with the schematic diagram shown in Fig. 1(a). To achieve the laser operation, the first-order grating is introduced into the surface ridge waveguide. To avoid light absorption from the metal contacts, there is no metallization on top of the ridge waveguide. Instead, n-metal contacts are laterally offset by 2 μm from the ridge as shown in the cross-sectional structure of the laser in Fig. 1(b). Therefore a thin ridge layer with high refractive index (higher than the average index of the active layer, as shown in Table 1) can be used and the grating can be etched shallowly but has a large overlap with the optical mode, therefore the grating can provide a strong coupling effect.

Table 1. Simplified Waveguide Structure

Layer	Material	Refractive index	Thickness (μm)
Upper cladding	AlGaAs	3.437	0.4
Active region	AlGaInAs	3.413	0.164
Lower cladding	AlGaAs	3.311	2.0
Substrate	GaAs	3.648	

As shown in Fig. 1(b), the proposed DFB laser is a surface ridge waveguide laser. At the same doping level, the n-doped layer has lower resistance because the mobility of electrons is much larger than holes. Therefore, the upper cladding layer is n-doped to reduce the sheet

Optics EXPRESS

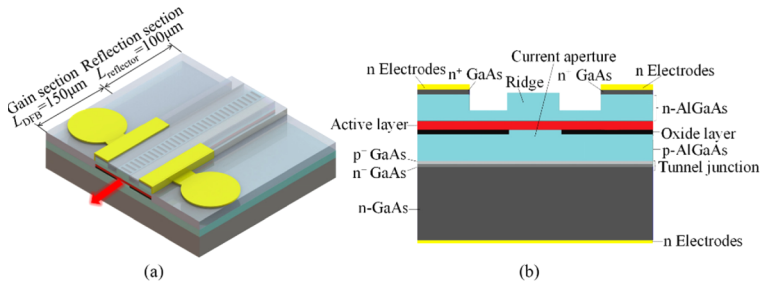

Fig. 1. Schematic diagrams of the proposed DFB laser: (a) top view, (b) cross section of the laser structure.

resistance. The junction is thus a n-i-p structure from the top to bottom. To facilitate the use of n-type substrate, we introduce a tunnel junction into the whole structure [31]. Therefore, the laser is based on an n-i-p-n epitaxial wafer structure. The active region consists of 0.5% compressively-strained (CS) InGaAs 5 quantum wells (QWs) and 4 $Al_{0.37}Ga_{0.63}As$ barriers sandwiched by two 60 nm-thick $Al_{0.37}Ga_{0.63}As$ confinement layers. The optical confinement factor Γ of the quantum wells is 0.0381. The MQWs have a photoluminescence (PL) peak around 837 nm. The high refractive index n-$Al_{0.25}Ga_{0.75}As$ is selected to be the n-doped upper cladding layer with a thickness of 400 nm to ensure the large optical confinement of the fundamental mode in the rib area. An n+-GaAs contact layer is then grown on top of the upper cladding layer. The p-doped lower cladding layer is p-$Al_{0.44}Ga_{0.56}As$ with a thickness of 2 μm. Just below the active region there is an $Al_{0.96}Ga_{0.04}As$ oxidation layer inserted into the lower cladding layer. An oxidation aperture will be formed afterwards to force current injected into the required region as shown in Figs. 1(a) and (b). The detailed parameters of the simplified structure are shown in Table 1 where the MQWs and confinement layers are simplified into one equivalent layer with the average index of around 3.413 and the thickness of 164 nm.

To obtain a low threshold, the two-section DFB laser structure [32–33] is used as shown in Fig. 1(a) to maintain a short laser cavity including the front gain section L_{DFB} = 150 μm and the back reflection section $L_{reflector}$ = 100 μm. Both sections are of the same epitaxial wafer structure and the grating extends the full length of the laser structure. The reflection section is just behind the gain section. The laser has just contacts only for the gain section. The n-contact area of the reflection section is etched off as shown in Fig. 1(a). This ensures that the current injection aperture in the reflection section is fully closed during the $Al_{0.96}Ga_{0.04}As$ oxidation process and therefore there is no current injection in this section. The integrated reflection section provides additional feedback [32], which helps the laser to improve the output efficiency. It also helps to extend the total chip length so as to facilitate the chip cleavage later on because the laser cavity is only 150 μm long. To achieve a high single mode yield, a quarter wavelength (λ/4) phase shift is introduced into the grating of the gain section of the designed DFB laser. The phase shift is optimized to be placed in the position around two-fifths of the active section closer to the back as analyzed in [33] to ensure a high output power and good side-mode suppression-ratio (SMSR).

2.2. Fabrication

The fabrication process of the proposed DFB laser is quite simple with the first-order gratings shallowly etched on the surface of the ridge waveguide, and the detailed process is shown in Figs. 2(a)–2(f). First, we selectively wet etched the contact layer n+-GaAs with citric acid: H_2O_2 to reduce the optical absorption of the waveguide as shown in Fig. 2(b). An electron beam lithography (EBL) was used to pattern first-order gratings with a 50% duty cycle. These gratings were transferred into a silicon dioxide (SiO_2) hard mask by inductively coupled plasma

Optics EXPRESS

reactive ion etching (ICP-RIE) using a gas mixture of CF_4/O_2. The gratings were further etched into the upper cladding layer by RIE etching with a gas mixture of $Cl_2/BCl_3/CH_4$ as shown in Fig. 2(c). The scanning electron microscopic (SEM) image of the fabricated first-order surface gratings is shown in Fig. 3(a). Next, the 2 μm-width ridge waveguide was patterned by i-line lithography, transferred into the silicon dioxide by ICP-RIE with CF_4/O_2, and etched into the upper cladding layer to a thickness of about 300 nm by ICP-RIE drying etching with a gas mixture of $Cl_2/BCl_3/CH_4$ as shown in Fig. 2(d).

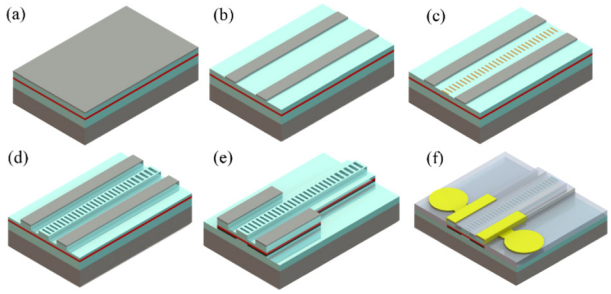

Fig. 2. Fabrication process of the proposed DFB laser: (a) the whole wafer, (b) selectively removing the top ohmic contact layer, (c) patterning the gratings, (d) etching the waveguide, (e) selective oxidation, (f) metallization.

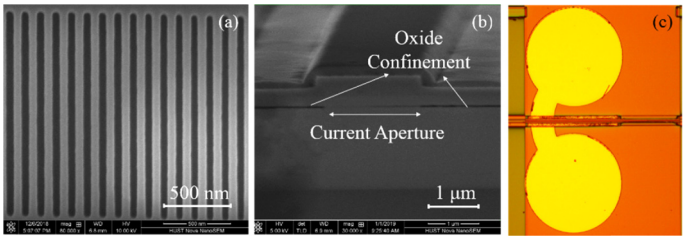

Fig. 3. Scanning electron microscopic (SEM) images of (a) the first-order surface gratings (b) the oxide-aperture for current confinement. (c) Microscope image of fabricated DFB laser.

Then, the oxidized region was also patterned by i-line lithography and etched by ICP-RIE etching using $Cl_2/BCl_3/Ar$ as shown in Fig. 2(e). The aluminum-rich $Al_{0.96}Ga_{0.04}As$ layer was oxidized by a mixed gas of N_2 and H_2O vapour at a temperature 455 °C to perform a current confined aperture. Each of the two sides of the oxidation region is oxidized to about 7 μm, and the average oxidation rate is about 0.135 μm/min. The scanning electron microscopic (SEM) images of the oxide-apertures for current confinement is shown in Fig. 3(b) where the dark line is the oxidized $Al_{0.96}Ga_{0.04}As$ layer. A current aperture is formed right below the ridge waveguide as shown in Fig. 3(b) which ensures high injection efficiency. The devices have current aperture of around 2 μm. Afterwards, top side N-electrodes Ge/Au/Ni/Au were evaporated on the contact layer by a lift-off process as shown in the Fig. 2(f). The epiwafer was thinned to ~150 μm and the backside electrode was realized by depositing Ge/Au/Ni/Au. Finally, the chips were cleaved into separate bars without facet coating.

3. Results and discussion

The fabricated devices were mounted on a simple Cu heat sink with the Thermo Electric Cooler (TEC) for testing. We first tested the FP lasers fabricated in the same run and from the same

Optics EXPRESS

epitaxial structure as the DFB lasers. The devices were tested at 20 °C with the cavity length L in the range from 300 μm to 500 μm of 50 μm intervals and at 1000 μm. Figure 4(a) shows the reciprocal of the differential quantum efficiency $1/\eta_d$ of the FP lasers as function of the cavity length L. According to the following expression in [34]:

$$\frac{1}{\eta_d} = \frac{\alpha_i}{\eta_i In(1/R)} L + \frac{1}{\eta_i} \tag{1}$$

and

$$\eta_d = \frac{e}{h\nu}\eta \tag{2}$$

where η_d is the differential quantum efficiency, $R = r_1 r_2$ is the mean reflectivity of the FP laser, α_i represent the net internal optical loss and and η_i is injection efficiency, η is the slope efficiency of the laser, e represent the elementary charge, h and ν represent the Planck constant and optical frequency, respectively.

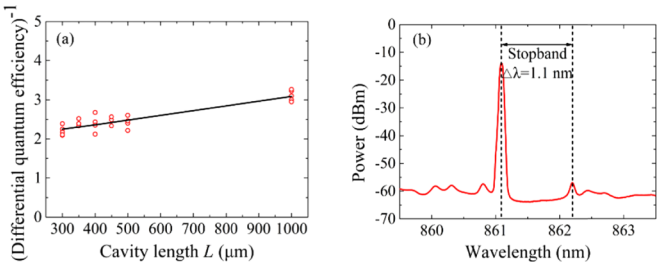

Fig. 4. (a) The reciprocal of measured efficiency versus cavity length of the FP lasers. (b) Measured optical spectrum of the test laser with uniform grating near threshold.

The reflectivity R of the laser is about 0.3. By the linear fitting the reciprocal of the slope efficiency $1/\eta_d$ versus the FP laser cavity length L, we can deduce the net internal optical loss α_i and the injection efficiency η_i which are about 7.84 cm^{-1} and 53.56%, respectively, from Fig. 4(a). The high internal loss and low injection efficiency were contributed from the fabrication quality and the unoptimized current aperture size, which in a result decreased the laser performance in terms of the threshold and slope efficiency as demonstrated later. The metal contacts are placed on both sides of the ridge waveguide. In this case, rather than directly injecting the current into the active region below the ridge waveguide like the conventional ridge waveguide DFB laser, the current has to spread in the ridge layer before vertically inject into the active layer, which will affect the injection efficiency of the laser. The current aperture can help improve the injection efficiency of the DFB laser. According to [35–36], the injection efficiency is largely determined by the size of the current aperture, with the decrease of the current aperture, the threshold of the laser decreases and the injection efficiency of laser increases within limits. So we can optimize the size of current aperture to improve the injection efficiency and thus the laser performance in future designs.

To extract the coupling coefficient of the surface gratings, we fabricated some test lasers with uniform surface grating which is distributed in the whole ridge waveguide and has the same period without introducing any additional phase shift. Since the spectral shape at threshold current is not affected by the loss and gain, we can get the stopband width $\Delta\lambda$ from the measured spectrum of the uniform grating lasers. The coupling coefficient then can be estimated based on the following relationship between it and the stopband width for the uniform grating lasers [37–38]:

$$\Delta\lambda = \frac{\lambda_B^2}{\pi n_g}\sqrt{(\pi/L)^2 + \kappa^2} \tag{3}$$

Optics EXPRESS

where, n_g is the group index of the waveguide and L is the grating length, $\Delta\lambda$ is the Bragg wavelength, κ is the coupling coefficient. We measured the optical spectrum of the fabricated lasers with uniform grating. The light output of the lasers was first coupled into a lensed single-mode fiber, and then connected to the optical spectrum analyser. Figure 4(b) shows the measured spectrum near threshold current for the 250 μm-long laser with uniform grating. It is found that the stopband width is about 1.1 nm and the Bragg wavelength is 861 nm as shown in Fig. 4(b). Therefore, the grating index-coupling coefficient of our devices is estimated to be 200 cm^{-1} by the above formula with the etching depth measured to be about 100 nm, which is much higher than the generally used gratings of lasers. Numerically, we also calculated the coupling coefficient of the grating in such a waveguide structure through the simulated transmission spectra using the 3D FDTD method. Figure 5(a) shows the calculated results versus the etching depth of the grating when the ridge waveguide height is 300 nm. It is obvious that the deeper etching depth, the larger coupling coefficient. When the etching depth is 250 nm, the coupling coefficient reaches 800 cm^{-1}. In that case, the threshold predicted is sub-milliampere theoretically for the proposed laser. However, the index-coupling coefficient of our fabricated devices is much lower than expected mainly caused by the imperfect etching profile with the tilt side walls and inappropriate duty cycle of the fabricated grating during the first run. The decreased coupling coefficient increased the threshold of the laser as demonstrated later.

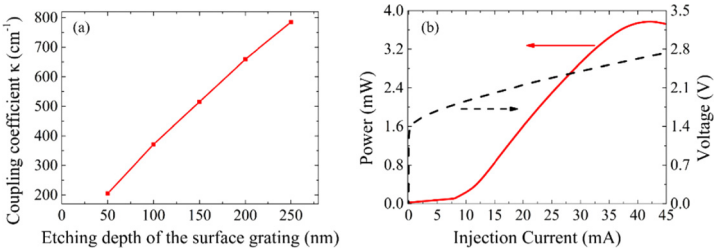

Fig. 5. (a) The calculated index-coupling coefficient as a function of depth of the etched grating. (b) Light output (solid line) and voltage (dashed line) versus injection current for the fabricated DFB laser.

The proposed surface grating DFB lasers were fabricated with the microscope image shown in the Fig. 3(c). The gain and reflection sections are 150 μm and 100 μm long, respectively. The width of the surface ridge waveguide is 2 μm. We characterized the fabricated bare lasers on a Cu heat sink with the TEC to control the devices' temperature. Figure 5(b) shows light output versus injection current (L-I) (solid line) and voltage versus current (V-I) (dashed line) characteristics at 20 °C.

Both facets of the fabricated DFB lasers are as-cleaved, and the output power was detected by a large-area Si detector from the facet close to the gain section. It is seen that a relatively low threshold current (I_{th}) of about 8 mA and a slope efficiency of about 0.16 mW/mA were obtained. As discussed before, if the injection efficiency and coupling coefficient are properly increased, we will get a lower threshold and higher slope efficiency. The differential series resistance and the turn on voltage were about 23 Ω and 1.5 V, respectively. According to a V-I characteristic between two n-type electrodes separated on both sides of ridge waveguide, the sheet resistance was roughly estimated to be about 1600 Ω/square which corresponds to about 46% of the total series resistance. The sheet resistance was high possibly resulted from the insufficient offset distance between the ridge waveguide and the n-contact metal, and also the unoptimized thickness of the transverse conductive layer $Al_{0.25}Ga_{0.75}As$. Figure 6(a) shows the output power of the DFB laser versus injection current for various operating temperature from 10 °C to 50 °C. Single mode operation was observed with the injection current up to 45 mA and without any mode hopping.

Optics EXPRESS

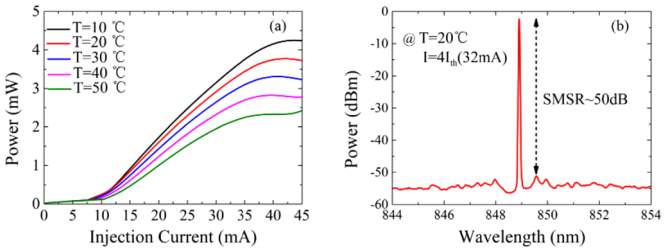

Fig. 6. (a) Light output versus injection current for the fabricated DFB laser at the temperature from 10 °C to 50 °C. (b) Lasing spectrum of the fabricated uncoated DFB laser at 20 °C when the bias current was 32 mA.

The output power is limited by thermal roll-over due to the poor heat conductance of the bare devices and the large series resistance mainly contributed by the contact resistance and sheet resistance. We can reduce the series resistance to improve the device performance by optimizing the gap between the ridge waveguide and the n-contact metal, the thickness of the sheet $Al_{0.25}Ga_{0.75}As$, and also the contact resistance in future designs.

The output spectrum of the fabricated two-section surface grating DFB lasers was also measured. The fabricated lasers show very good single mode operation with the side mode suppression ratio (SMSR) ~ 50 dB as shown in Fig. 6(b) with the injected current of 32 mA around 4 times threshold at the temperature of 20 °C.

Figure 7(a) shows the measured spectra for different bias currents of 15 mA, 25 mA, 35 mA, 45 mA at 20 °C. Stable single-mode operation was observed with SMSR greater than 42 dB. The lasing wavelength was 850.3 nm at 45 mA. The bare devices suffered from heat dissipation problem, i.e., with the injection of current, the temperature of the device especially the active region increases, thus the band gap becomes narrower, which leads to the increase of refractive index in active region. So that the emission wavelength of the fabricated laser red shifted as a function of the injection current as shown in Fig. 7(b). The variation of emission wavelength with injection current, $\Delta\lambda/\Delta I$, is around 0.08 nm/mA.

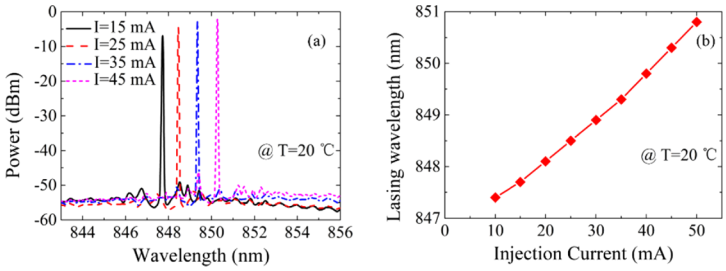

Fig. 7. (a) Lasing spectra of the fabricated uncoated DFB laser at 20 °C when the bias current increased from 15 mA to 45 mA. (b) The emission wavelength shift as a function of injection current at 20 °C.

As shown in Fig. 8(a), the fabricated laser worked with single mode operation at 25 mA over the temperature range from 10 to 50 °C. The Fig. 8(b) shows the emission wavelength shift as a function of stage temperature at injection current 25 mA. The variation of emission wavelength with temperature, $\Delta\lambda/\Delta T$, is around 0.06 nm/°C. It is assumed that the electrical input power is almost converted to thermal power except for the output optical power. Considering the lasing-wavelength as a function of active region (stage) temperature ($\Delta\lambda/\Delta T$) and the shift in emission wavelength as a function of thermal power ($\Delta\lambda/\Delta P$) [39], the thermal resistance

Optics EXPRESS

$Z_T = (\Delta\lambda/\Delta T)^{-1}(\Delta\lambda/\Delta P)$ was estimated to be around 447 K/W for the fabricated DFB lasers. The thermal resistance is higher than most typical semiconductor lasers, but it is much lower than VCSELs [40]. This will limit the laser performance especially at high temperatures. We believe that the laser performance can be greatly improved by soldering the laser to heat-sink structures, integrating some heat dissipation structures. In addition, we can further reduce differential series resistance by optimizing the fabrication process and the laser structure.

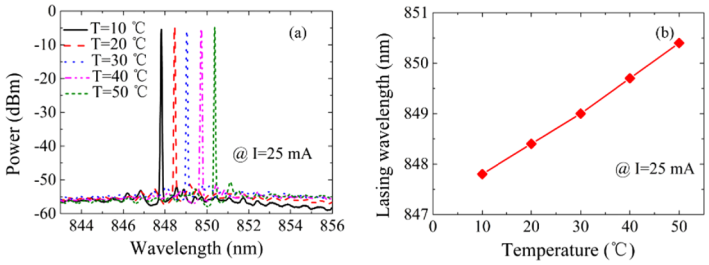

Fig. 8. (a) Lasing spectra of the fabricated uncoated DFB laser at a bias current of 25 mA when the temperature is increased from 10 to 50 °C. (b) The emission wavelength shift as a function of the stage temperature at 25 mA.

4. Conclusion

In conclusion, we demonstrated, for the first time, in the GaAs/AlGaAs material system, a DFB laser with a first-order surface grating etched into the surface ridge waveguide. There is no metal contacts on the surface ridge waveguide, the n-metal contacts are placed on the both sides of the ridge waveguide instead to remove the absorption of the metal contacts. The thin ridge layer is allowed to be used with relatively higher refractive index compared to the active layer; therefore the grating can be shallowly etched but provides a strong coupling effect. The oxidation aperture forces the current to flow through the active region right below the ridge waveguide, which is crucial to improve the injection efficiency of the laser. These insure that the proposed laser can work with low threshold at a short cavity length. The index-coupling coefficient reaches 200 cm^{-1} for the etched grating with a depth of only about 100 nm which is much higher than the generally used gratings of lasers. However, it is much lower than expected mainly caused by the imperfect etching profile with the tilt side walls and inappropriate duty cycle of the fabricated grating. The fabricated 150 μm-long DFB laser exhibited a relatively low threshold current of 8 mA and single-mode operation with a side mode suppression ratio (SMSR) up to 50 dB at the injected current of 32 mA at 20 °C. Stable single mode operation has been observed for the fabricated DFB laser over the temperature range from 10 to 50 °C. Compared to VCSELs, the SMSR of the laser in this work is higher while the performance in terms of the threshold and output power is worse. We think the reason is that the coupling coefficient of the fabricated grating is lower than expected The thermal resistance is higher than most typical semiconductor lasers due to the high sheet resistance, the high contact resistance and no good heat-sinking, which also affects the expected performance of the fabricated lasers. In the future, to improve the laser performance, we can further thin the ridge layer with higher refractive index and optimize the fabrication process of gratings to obtain a greater coupling coefficient. In addition, we can optimize the distance between the ridge waveguide and the n-contact metal as well as the thickness of the transverse conductive layer to reduce the differential series resistance, and the size of current aperture to improve the injection efficiency. The theoretical prediction shows that when the index-coupling coefficient reaches 800 cm^{-1}, the threshold current will be below 1 mA and the modulation bandwidth should reach 25 GHz in this proposed DFB laser. Thus we believe that the proposed laser scheme will be a potential low threshold DFB laser scheme combines the advantages of

Optics EXPRESS

both DFB lasers and VCSELs. In addition, the laser is regrowth free, thus has advantages of low cost and high reliability.

Funding

National Natural Science Foundation of China (61675077, 61875066, 61861136001); State Key Laboratory on Integrated Optoelectronics (IOSKL2017KF14); Science Foundation Ireland (15/IA/2854, 13/RC/2077); Science Foundation Ireland - National Natural Science Foundation of China Partnership Programme 2017(17/NSFC/4918)

References

1. P. Gill, "When should we change the definition of the second?" Phil. Trans. R. Soc. A **369**(1953), 4109–4130 (2011).
2. T. Rosenband, D. B. Hume, P. O. Schmidt, C. W. Chou, A. Brusch, L. Lorini, W. H. Oskay, R. E. Drullinger, T. M. Fortier, J. E. Stalnaker, S. A. Diddams, W. C. Swann, N. R. Newbury, W. M. Itano, D. J. Wineland, and J. C. Bergquist, "Frequency ratio of Al+ and Hg+ single-ion optical clocks; metrology at the 17th decimal place," Science **319**(5871), 1808–1812 (2008).
3. N. Yu, J. M. Kohel, J. R. Kellogg, and L. Maleki, "Development of an atom-interferometer gravity gradiometer for gravity measurement from space," Appl. Phys. B: Lasers Opt. **84**(4), 647–652 (2006).
4. X. Lu, D. Zibar, and I. T. Monroy, "24-Dimensional Rate-Flexible Carrierless and Amplitude Phase Modulation for 100G IM-DD Transmission Using 850 nm VCSEL," *Proc. Eur. Conf. Opt. Commun*, 1–3 (2018).
5. H. Liu, G. Gredat, G. Baili, F. Gutty, F. Goldfarb, I. Sagnes, and F. Bretenaker, "Noise investigation of a dual-frequency VECSEL for application to cesium clocks," J. Lightwave Technol. **36**(18), 3882–3891 (2018).
6. X. Liu, E. Ivanov, V. I. Yudin, J. Kitching, and E. A. Donley, "Low-drift coherent population trapping clock based on laser-cooled atoms and high-coherence excitation fields," Phys. Rev. A **8**(5), 054001 (2017).
7. O. Carraz, F. Lienhart, R. Charrière, M. Cadoret, N. Zahzam, Y. Bidel, and A. Bresson, "Compact and robust laser system for onboard atom interferometry," Appl. Phys. B: Lasers Opt. **97**(2), 405–411 (2009).
8. A. R. Nehrir, K. S. Repasky, and J. L. Carlsten, "Eye-safe diode-laser-based micropulse differential absorption lidar (DIAL) for water vapor profiling in the lower troposphere," J. Atmos. Oceanic Technol. **28**(2), 131–147 (2011).
9. D. L. Huffaker, D. G. Deppe, K. Kumar, and T. J. Rogers, "Native-oxide defined ring contact for low threshold vertical cavity lasers," Appl. Phys. Lett. **65**(1), 97–99 (1994).
10. G. M. Yang, M. H. Macdougal, and P. D. Dapkus, "Ultralow threshold current vertical-cavity surface-emitting lasers obtained with selective oxidation," Electron. Lett. **31**(11), 886–888 (1995).
11. F. Gruet, A. Al-Samaneh, E. Kroemer, L. Bimboes, D. Miletic, C. Affolderback, D. Wahl, R. Boudot, G. Mileti, and R. Michalzik, "Metrological characterization of custom-designed 894.6 nm VCSELs for miniature atomic clocks," Opt. Express **21**(5), 5781–5792 (2013).
12. J. Zhang, X. Zhang, H. Zhu, J. Zhang, Y. Ning, L. Qin, and L. Wang, "High-temperature operating 894.6nm-VCSELs with extremely low threshold for Cs-based chip scale atomic clocks," Opt. Express **23**(11), 14763–14773 (2015).
13. S. K. Serkland, G. M. Peake, K. M. Geib, R. Lutwak, R. M. Garvey, M. Varghese, and M. Mescher, "VCSELs for atomic clocks," Proc. of SPIE **6132**, 613208 (2006).
14. P. Debernardi, J. M. Ostermann, M. Feneberg, C. Jalics, and R. Michalzik, "Reliable polarization control of VCSELs through monolithically integrated surface gratings: a comparative theoretical and experimental study," IEEE J. Sel. Top. Quantum Electron. **11**(1), 107–116 (2005).
15. A. A-Samaneh, S. Renz, A. Strodl, W. Schwarz, D. Wahl, and R. Michalzik, "Polarization-stable single-mode VCSELs for Cs-based MEMS atomic clock applications," Proc. SPIE **7720**, 772006 (2010).
16. A. Klehr, M. Braun, F. Bugge, G. Erbert, J. Fricke, A. Knauer, P. Ressel, H. Wenzel, and G. Trankle, "High-power ridge-waveguide and broad-area lasers with a DFB resonator in the wavelength range 760–790 nm," Proc. SPIE **5738**, 416–424 (2005).
17. C. Cayron, M. Tran, Y. Robert, M. Lecomte, O. Parillaud, M. Garcia, and M. Krakowski, "High power distributed feedback and Fabry-Perot Al-free laser diodes at 780 nm for Rubidium pumping," Proc. SPIE **7953**, 79530A (2011).
18. N. V. Bandel, M. Garcia, M. Lecomte, A. Larrue, Y. Robert, E. Vinet, and R. Matthey, "DFB-ridge laser diodes at 894 nm for Cesium atomic clocks," Quantum Sensing and Nano Electronics and Photonics XIII **9755**, 97552K (2016).
19. L. M. Miller, J. T. Verdeyen, J. J. Coleman, R. P. Bryan, J. J. Alwan, K. J. Beernink, J. S. Hughes, and T. M. Cockerill, "A distributed feedback ridge waveguide quantum well heterostructure laser," IEEE Photonics Technol. Lett. **3**(1), 6–8 (1991).
20. R. D. Martin, S. Forouhar, S. Keo, R. J. Lang, R. G. Hunsperger, R. C. Tiberio, and P. F. Chapman, "CW performance of an InGaAs-GaAs-AlGaAs laterally-coupled distributed feedback (LC-DFB) ridge laser diode," IEEE Photonics Technol. Lett. **7**(3), 244–246 (1995).
21. B. Corbett and D. McDonald, "Single longitudinal mode ridge waveguides 1.3 μm Fabry-Perot laser by modal perturbation," Electron. Lett. **31**(25), 2181–2182 (1995).

Optics EXPRESS

22. R. M. Lammert, J. S. Hughes, S. D. Roh, M. L. Osowski, A. M. Jones, and J. J. Coleman, "Low-threshold narrow-linewidth InGaAs-GaAs ridge-waveguide DBR lasers with first-order surface gratings," IEEE Photonics Technol. Lett. **9**(2), 149–151 (1997).
23. J. W. Zimmerman, R. K. Price, U. Reddy, N. L. Dias, and J. J. Coleman, "Narrow linewidth surface-etched DBR lasers: fundamental design aspects and applications," IEEE J. Sel. Top. Quantum Electron. **19**(4), 1503712 (2013).
24. A. Abdullaev, Q. Lu, W. Guo, M. J. Wallace, M. Nawrocka, F. Bello, A. Benson, J. O'Callaghan, and J. F. Donegan, "Improved performance of tunable single-mode laser array based on high-order slotted surface grating," Opt. Express **23**(9), 12072–12078 (2015).
25. J. Telkkälä, J. Viheriälä, A. Laakso, K. Leinonen, J. Lyytikäinen, J. Karinen, and M. Pessa, "Distributed feedback laser diodes emitting at 894 nm suitable for atomic clock applications fabricated using nanoimprint lithography," *Conference on Lasers and Electro-Optics* (Optical Society of America, 2010), paper JTuD102.
26. Y. Ding, G. Ternent, A. Saeed, C. J. Hamilton, N. Hempler, G. P. A. Malcolm, G. T. Maker, M. Sorel, and D. J. Paul, "GaAs-based distributed feedback laser at 780 nm for 87 Rb cold atom quantum technology," *Proc. Conf. Lasers Electro-Opt./Eur. Eur. Quantum Electron. Conf.*, 1 (2017).
27. H. Virtanen, T. Uusitalo, M. Karjalainen, S. Ranta, J. Viheriälä, and M. Dumitrescu, "Narrow-Linewidth 780-nm DFB Lasers Fabricated Using Nanoimprint Lithography," IEEE Photonics Technol. Lett. **30**(1), 51–54 (2018).
28. H. Wenzel, J. Fricke, J. Decker, P. Crump, and G. Erbert, "High-power distributed feedback lasers with surface gratings: Theory and experiment," IEEE J. Sel. Top. Quantum Electron. **21**(6), 352–358 (2015).
29. T. T. Shindo, T. Okumura, H. Ito, T. Koguchi, D. Takahashi, Y. Atsumi, J. Kang, R. Osabe, T. Amemiya, N. Nishiyama, and S. Arai, "Lateral-current-injection distributed feedback laser with surface grating structure," IEEE J. Sel. Top. Quantum Electron. **17**(5), 1175–1182 (2011).
30. D. Inoue, J. Lee, T. Hiratani, Y. Atsuji, T. Amemiya, N. Nishiyama, and S. Arai, "Sub-milliampere threshold operation of butt-jointed built-in membrane DFB laser bonded on Si substrate," Opt. Express **23**(6), 7771–7778 (2015).
31. H. Venghaus and N. Grote, *Fibre optic communication: key devices*, 2nd ed., 161. Springer (2017).
32. G. Liu, G. Zhao, J. Sun, D. Gao, Q. Lu, and W. Guo, "Experimental demonstration of DFB lasers with active distributed reflector," Opt. Express **26**(23), 29784–29795 (2018).
33. G. Zhao, J. Sun, Y. Xi, D. Gao, Q. Lu, and W. Guo, "Design and simulation of two-section DFB lasers with short active-section lengths," Opt. Express **24**(10), 10590–10598 (2016).
34. L. A. Coldren, S. W. Corzine, and M. L. Mashanovitch, *Diode Lasers and Photonic Integrated Circuits*, 218, (John Wiley and Sons, 2012).
35. H. J. Unold, S. W. Mahmoud, R. Jaeger, M. Golling, M. Kicherer, F. Mederer, M. C. Riedl, T. Knödl, M. Miller, R. Michalzik, and K. J. Ebeling, "Single-mode VCSELs," *International Society for Optics and Photonics* 4649 (2002).
36. H. Li, P. Wolf, P. Moser, G. Larisch, J. A. Lott, and D. Bimberg, "Temperature-stable, energy-efficient, and high-bit rate oxide-confined 980-nm VCSELs for optical interconnects," IEEE J. Sel. Top. Quantum Electron. **21**(6), 405–413 (2015).
37. J. Buus, M.-C. Amann, and D. J. Blumenthal, *Tunable Laser Diodes and Related Optical Sources*, 2nd ed., (Wiley-Interscience, 2005).
38. N. Matuschek, F. X. Kartner, and U. Keller, "Exact coupled-mode theories for multilayer interference coatings with arbitrary strong index modulations," IEEE J. Quantum Electron. **33**(3), 295–302 (1997).
39. M. N. Sysak, H. Park, A. W. Fang, J. E. Bowers, R. Jones, O. Cohen, O. Raday, and M. J. Paniccia, "Experimental and theoretical thermal analysis of a Hybrid Silicon Evanescent Laser," Opt. Express **15**(23), 15041–15046 (2007).
40. A. N. Al-Omari, G. P. Carey, S. Hallstein, J. P. Watson, G. Dang, and K. L. Lear, "Low thermal resistance high-speed top-emitting 980-nm VCSELs," IEEE Photonics Technol. Lett. **18**(11), 1225–1227 (2006).